Since January 2020 Elsevier has created a COVID-19 resource centre with free information in English and Mandarin on the novel coronavirus COVID-19. The COVID-19 resource centre is hosted on Elsevier Connect, the company's public news and information website.

Computers in Biology and Medicine 145 (2022) 105468

Contents lists available at ScienceDirect

Computers in Biology and Medicine

journal homepage: www.elsevier.com/locate/compbiomed

Phytochemicals-based targeting RdRp and main protease of SARS-CoV-2 using docking and steered molecular dynamic simulation: A promising therapeutic approach for Tackling COVID-19

Arpana Parihar [a,*], Zannatul Ferdous Sonia [b], Farjana Akter [b], Md Ackas Ali [b], Fuad Taufiqul Hakim [b], Md Shahadat Hossain [b]

[a] Industrial Waste Utilization, Nano and Biomaterials, CSIR-Advanced Materials and Processes Research Institute (AMPRI), Hoshangabad Road, Bhopal, 462026, MP, India

[b] Division of Infectious Diseases and Division of Computer-Aided Drug Design, The Red-Green Research Centre, BICCB, 16 Tejkunipara, Tejgaon, Dhaka, 1215, Bangladesh

ARTICLE INFO

Keywords:
COVID-19
Molecular dynamic simulation
Steered dynamic simulation
RdRp
Main proteases
Phytochemicals

ABSTRACT

The ongoing COVID-19 pandemic has affected millions of people worldwide and caused substantial socio-economic losses. Few successful vaccine candidates have been approved against SARS-CoV-2; however, their therapeutic efficacy against the mutated strains of the virus remains questionable. Furthermore, the limited supply of vaccines and promising antiviral drugs have created havoc in the present scenario. Plant-based phytochemicals (bioactive molecules) are promising because of their low side effects and high therapeutic value. In this study, we aimed to screen for suitable phytochemicals with higher therapeutic value using the two most crucial proteins of SARS-CoV-2, the RNA-dependent RNA polymerase (RdRp) and main protease (Mpro). We used computational tools such as molecular docking and steered molecular dynamics simulations to gain insights into the different types of interactions and estimated the relative binding forces between the phytochemicals and their respective targets. To the best of our knowledge, this is the first report that not only involves a search for a therapeutic bioactive molecule but also sheds light on the mechanisms underlying target inhibition in terms of calculations of force and work needed to extractthe ligand from the pocket of its target. The complexes showing higher binding forces were subjected to 200 ns molecular dynamic simulations to check the stability of the ligand inside the binding pocket. Our results suggested that isoskimmiwallin and terflavin A are potential inhibitors of RdRp, whereas isoquercitrin and isoorientin are the lead molecules against Mpro. Collectively, our findings could potentially aid in the development of novel therapeutics against COVID-19.

1. Introduction

Globally, the coronavirus disease (COVID-19) pandemic has been devastating and has caused enormous socio-economic losses. The lack of resources and preparedness to deal with the pandemic has already claimed millions of lives and left billions of people severely affected. On March 11, 2020, the COVID-19 outbreak was declared a pandemic by the World Health Organization (WHO), and up to January 29, 2022, over 364,191,494 cases and 5,631,457 deaths were reported [1–4]. Severe acute respiratory syndrome coronavirus 2 (SARS-CoV-2) is the causative agent of COVID-19 and is closely linked with SARS-CoV, which was responsible for the 2002–2003 pandemic [2]. SARS-CoV-2 is an RNA virus with a genome comprising 29,903 nucleotides, a single-stranded positive-sense RNA encoding five key structural proteins, namely spike (S), envelope (E), membrane (M), nucleocapsid (N), and ORF1ab, and 16 non-structural proteins [3]. Severe upper respiratory complexities resulting in acute/chronic pneumonia and bronchiolitis are caused by SARS-CoV-2. The spike protein is a homotrimeric glycoprotein situated on the virion surface that facilitates the entry of the virus through its binding to the angiotensin-converting enzyme 2 (ACE2) receptor, frequently present in the upper respiratory tract [5]. Few successful vaccine candidates have been approved; however, as the virus mutates at a much faster rate, the efficacy of vaccines against mutated strains has not yet been proven [6–9]. The second wave of the

* Corresponding author.
E-mail address: arpana_parihar@yahoo.com (A. Parihar).

https://doi.org/10.1016/j.compbiomed.2022.105468
Received 29 September 2021; Received in revised form 27 March 2022; Accepted 27 March 2022
Available online 30 March 2022

pandemic was due to new strains of SARS-CoV-2, which were reported first in the UK (N501Y), South Africa (K417N-E484K–N501Y), and Brazil (K417T-E484K–N501Y), have higher infectivity, associated mortality, and morbidity [8]. To date, only a few drugs, such as remdesivir, favipiravir, and ivermectin, have shown potential for the treatment of COVID-19. However, their response varies from person to person, and a limited supply of these drugs has created worldwide havoc [10–15]. The social and economic burdens due to COVID-19 and the possibility of the occurrence of future pandemics have resulted in a pressing need for the rapid development of therapeutics and medicinal interventions. Given the current scenario, new candidate drugs that exhibit lower side effects with a maximum therapeutic potential need to be examined. Plant-based phytochemicals are bioactive molecules that are promising candidates owing to their low side effects and high therapeutic value. The two main targets for drug design against SARS-CoV-2 are RNA-dependent RNA polymerase (RdRp) and the main protease (Mpro) [16,17]. RdRp is an essential enzyme for viral RNA replication, while Mpro is responsible for the generation of viral proteins and assembly. Inhibiting these two targets can potentially hamper the growth of SARS-CoV-2, thereby preventing or reducing the spread of the virus before a drug/vaccine is available. Several studies have demonstrated the efficacy of phytochemicals, such as flavonoids, anisotine, and other natural molecules, for the treatment of COVID-19 infection [18–22]. A recent study reports the RdRp inhibitory potential of FDA-approved phytochemicals that can be used to treat COVID-19 [23]. In the present study, we aimed to screen plant-based natural molecules (approximately 1064) for their inhibitory effects against RdRp and Mpro using an *in silico* molecular docking approach. In addition, we intended to use steered molecular dynamics (SMD) simulation to estimate the relative binding forces and obtain insights into the interactions of phytochemicals with their respective targets. To the best of our knowledge, this is the first study that not only involves the search for therapeutic bioactive molecules but also sheds light on the mechanisms underlying target inhibition. The complexes that exhibited higher binding forces were subjected to 100 ns molecular dynamic simulations to check the stability of the ligand along with other features, including conformational flexibility, charge distribution, and solvent role in target recognition and binding to the inside of the active site pocket. The combinatorial approach using SMD and interaction energy calculations with molecular dynamics simulations is robust in shedding light on target-ligand interactions. Our results suggested that isoskimmiwallin and terflavin A are potential inhibitors of RdRp, whereas isoquercitrin and isoorientin are the lead molecules against Mpro. Taken together, our robust *in silico* approach has the potential for *in vitro* and *in vivo* extrapolation and could thus pave the way toward the development of novel therapeutics against COVID-19.

2. Methods

2.1. Protein preparation and ligand preparation

The crystal structure of RNA Dependent RNA polymerase (RdRp) and Main protease (Mpro) was downloaded from the RCSB PDB databank (PDB ID 6M71 and 6LU7). These proteins were prepared using the Protein preparation wizard of Maestro in Schrodinger's suite [24]. The proteins were prepared by correcting bonds, removing unrelated chemical complexes, eliminating water molecules from het groups, filling in missing side chains & loops creating zero-order bonds to metal atoms, the addition of hydrogen bonds, conversion of selenomethionine to methionine, and generating het states utilizing Epik. The maestro uses the PROPKA module for the generation of protonation states of amino acids at pH 7.4 to simulate physiological conditions. The protein structure minimization was done under the OPLS3e force field which optimized the protein hydrogen bonds via overlying followed by minimization [24–26]. The active site for binding the ligand molecules is the most important step for protein-ligand interaction. For this, the grid generation was done with the selection of a co-crystal ligand in the target protein. While generating the grid, the OPLS3e force field was used which creates a partial cut-off charge of 0.25 Å. The default parameters of 1 Å radii of Van der Waal's scaling factor were set for mounting the protein atoms [24]. A radius of 15°A around the control remdesivir-bound site was defined to perform molecular docking. A grid box was generated around the (RdRp) polymerase active site (the (A-G) conserved motifs) of the protein where the center was X: 126.174, Y: 130.592and Z: 129.7033 and the dimensions used were X: 44.7514, Y: 44.5709 and Z: 35.2935 in the search space as previously reported [27]. For grid generation in the case of Mpro, the information of the catalytic active site and substrate binding site residues coordinates was used as −12.0, 18.0, 65.0 Å along X-, Y-, and Z-axes, respectively whereas the dimension was considered as 26 × 28 × 30 Å respectively. During grid generation, careful inspection and confirmation of catalytic site residues (such as His41 and Cys145) and substrate binding site residues at an active site within the grid box were carried out [28]. The output of molecular docking poses generated for each ligand against the respective targets were ranked and selected among ligand-protein complex based on the docking scores.

Phytochemicals with antiviral, antimicrobial, and antioxidant properties were screened based on the literature survey and 3D structures of 645 molecules which were downloaded from the PubChem database [29]. The library of molecules was prepared using the LigPrep module of Maestro. This module generates different combinations of enantiomers and tautomers of ligands therefore the total number of ligand molecules increased up to 1064. Further, the protonation states of the ligand at pH 7.4 were adjusted by the Epik module [30]. Afterward, the LigPrep module utilizes the OPLS3e field for subsequent ligand preparation. This module prepares ligands with appropriate parameters such as optimization, determination of promoters, tautomers, 2D to 3D conversion, ionization state at pH 7.0, ring confirmation, and correction of partial atomic charges [30].

2.2. Molecular docking

The sequential multistep molecular docking study was performed to check the binding efficacy of the phytochemicals with RdRp and Mpro. The high throughput virtual screening (HTVS) based docking was done against RdRp and Mpro to screen the most appropriate ligands from the library which exhibit higher binding affinity towards the respective targets using flexible docking parameters using Schrodinger's Glide module. The top 10% of the ligands from the HTVS docking were selected for the standard precision (SP) docking procedure using Glide. Afterward, the top 20% of ligands from SP docking which display higher binding scores were selected and subjected to extra precision (XP) docking. Further, to calculate binding free energy (DG bind), the molecular mechanics generalized Born surface area (MM-GBSA) procedures [31] of the prime module were used [32–34]. The Maestro (Schrodinger) was used for all docking calculations, generation of the 3D structure of the protein model, 2D structures of molecules, and interactive maps. The values of inhibition constant (pKi), the negative logarithm of inhibition constants were calculated from the ΔG, obtained from the docking study using the following formula (1).

$$\Delta G = RT\,(\mathrm{Ln}Ki_{\mathrm{pred}}) \tag{1}$$

$$Ki_{\mathrm{pred}} = {}^{(\Delta G/RT)} \tag{2}$$

$$pKi = -(Ki_{\mathrm{pred}}) \tag{3}$$

where ΔG is binding affinity (kcal/mol), T stands for temperature that is 298.15 K, and R is a gas constant with 1.9872036 cal*(mol*K)$^{-1}$. Ki_{pred} is the inhibitory constant which primarily tells about the ability of a compound as a potential inhibitor. Further, the ADMET profile of the top 5 bioactive phytochemicals was analyzed using the ADMETsar server [32].

2.3. Steered molecular dynamic simulations

Steered molecular dynamic simulation was performed on the 5 best ligand-receptor complexes which have higher docking scores including one control against each protein (Mpro, PDB ID: 6LU7; RdRp, PDB ID: 6M71). The process is implemented by applying a time-dependent external force on the ligand to dissociate it from the protein-ligand complex. The YASARA steered molecular dynamics protocol [36] is chosen to simulate physiological conditions. The AMBER14 force field [37], the solvent density of 0.99,7, and pH of 7.4 at temperature 298K were used to exhibit a physiological system. Water solvent and Na^+/Cl^- ions (0.9%) were also added to this system. Periodic boundary conditions with cuboid box size for Mpro and 40 Å box size for RdRp were incorporated to perform the simulation. The initial energy minimization for each system was performed employing the steepest gradient approach (5000 cycles). Here, the simulation temperature was controlled using the Berendsen thermostat, and the pressure was kept constant throughout the simulation process. Multiple time-step algorithms were utilized, where the overall equilibration time was chosen as 3ps. The starting pulling accelerations were 200 p.m./ps^2 and 300 p.m./ps^2 for Mpro and RdRp, respectively. A time step of 1.25 fs was maintained in the process and the simulation trajectory was generated every 1ps. The maximum pulling length was chosen to be 17 Å for Mpro and 33 Å for RdRp, which ensured the complete solvation of the ligand while it was outside the protein cavity. The acceleration was applied at the center of mass of the ligand, while the axis was formed by the center of mass of the protein cavity. Besides acceleration data, this protocol also provides the force subjected to the ligand concerning the time of simulation and the distance of dislocation from the target. The average force profile was calculated by averaging the outcomes of 3 independent runs of each protein-ligand complex for both of the proteins. The calculation was done as follows:

$$F(t) = \frac{1}{N}\sum_{i=1}^{N} F_i(t)$$

Work was also calculated until the point beyond which no interactions persisted between the ligand-protein complex. Since work is a path function, i.e., dW = g(x) dx, where g(x) is the function of force subjected to the ligand concerning its dissociation, the total amount of work until the ligand is fully dissociated from protein can be calculated using the following formula

$$\int_0^{w_{dissc}} dw = \int_0^{x_{dissc}} g(x)dx$$

Integrating, $W_{dissc} = \int_0^{x_{dissc}} g(x)dx$

Where W_{dissc} is the work done to pull away the ligand and x_{dissc} is the distance at which the pulling process occurs. g(x) is obtained from the output from the YASARA protocol. An in-house script in OCTAVE has been developed which upon running calculates the work.

2.4. Molecular dynamics simulations

An MD system consisted of protein, one docked ligand, and water molecules were used. The 200 ns MD simulation was performed for RNA-dependent RNA polymerase (RdRp) (PDB ID- 6M71) and main protease (Mpro) (PDB ID- 6LU7), and four protein-ligand complexes by employing the program YASARA [38]. The complex was placed in a cuboid box and energetically minimized using the step-down algorithm with 5000 steps. The total charge of the system was neutralized by adding 0.9% NaCl at physiological pH 7.4. The AMBER14 force field was applied [37]]. Afterward, The Particle Mesh Ewald (PME) summation [39] was used to gain the long-range electrostatic interactions. The systems were balanced at 298K temperature which was controlled using the Berendsen thermostat [40] and standard pressure (1.01325 bar) for 100 ps using NPT (constant Number of particles, Pressure, and Temperature) ensembles. Finally, a period of 200 ns MD simulation was carried out with 1.25 fs 6-time steps [41]. Altogether, 2000 trajectories of the MD simulation were generated for further analysis.

After that, we calculated Principal Component Analysis, or PCA, by taking the last 100 ns of MD trajectory data. It is a dimensionality-reduction method that is often used to reduce the dimensionality of large data sets, by transforming a large set of variables into a smaller one that still contains most of the information in the large set. Any structural quality change during MD can be characterized by comparing different drug-protein complexes using PCA [22]. PCA tries to put maximum possible information in the first component, then maximum remaining information in the second, and so on, and thus generate a scree plot. An autoscale function was used to preprocess data [42]. For all calculations, we used the R platform [43] employing in-house developed codes. Plots were generated through the package ggplot2 [44]. The following equation contains the important components of a PCA model:

$$X = T_K P_K^T + E$$

where, the X matrix is expressed as a product of two new matrices, i.e TK and PK, TK serves as the matrix of scores that represents how samples relate to each other, PK represents the matrix of loadings which contain information about how variables relate to each other, k is the number of factors included in the model, and E is the matrix of residuals [45]. The molecular dynamic simulations were performed twice for all complexes in order to confirm the consistency of the results.

3. Results

3.1. Virtual screening and molecular docking

The interaction of key active site amino acid residues of protein target with the ligand molecule helps in designing and screening of potent drug molecules using the molecular docking method. The molecular docking results which include docking score, pKi, interacting amino acid, distance, bond category, and type of bond of 5 selected ligands with RdRp and Mpro have been enlisted in Table 1. One thousand sixty-four phytochemical molecules were screened and docked against the RdRp and Mpro. After virtual screening and HTVS, SP and XP molecular docking steps top 20 compounds were selected for each target protein respectively. Based on the analysis of binding interaction, binding affinity, and pKi values we have selected 5 potential ligands for each protein target for evaluation of the ADMET profile [35]. The molecular weight, number of H-bond acceptor/donor, rotatable bonds, human intestinal absorption, blood-brain barrier, mutagenesis, water-solubility, plasma protein binding ability, TPSA, and Log P value of lead hits have been listed in Supplementary Table 1. For evaluation of binding force between lead molecules against Mpro and RdRp, steered dynamic simulation was performed.

3.2. Steered molecular dynamic simulation

The five best ligand-protein complexes were chosen against each protein (PDB ID: 6LU7 and 6M71) subjected to steered molecular dynamic simulation (SMD). This method provides the force concerning the time of simulation and the distance of dislocation of the ligand from the active site. The average force profile was calculated by averaging the outcomes of three independent runs of SMD of each protein-ligand complex. The F_{max} (maximum force obtained during the unbinding process) of every complex was shown in Table 2. Here, work was calculated until the point beyond which no interactions persisted between the ligand-protein complex, and finally, the average work was calculated from three independent runs of each complex. Maximum work (W_{max}) done by ligand during the simulation was enlisted in

Table 1
Molecular docking score, interacting amino acid, distance, bond category, type of bond, and 2D interaction diagram of 5 selected ligands with RdRp and Mpro followed by Molecular docking.

Protein	Drug	Molecular Docking Score	pKi	Type of Interacting amino acid	Distance	Bond Category	Bond Type
Mpro	Isoquercitine	−10.432	7.6	ASN142	2.79947	H-Bond	Conventional
				GLU166	2.225	H-Bond	Conventional
				PRO168	2.68466	H-Bond	Carbon H-Bond
				HIS41	5.20104	Hydrophobic	Pi-Pi T-shaped
	Arborside	−9.979	7.3	ASN142	3.00384	H-Bond	Conventional
				ASN142	1.88505	H-Bond	Conventional
				GLN189	2.2028	H-Bond	Conventional
				PRO168	2.77701	H-Bond	Carbon H-Bond
				HIS41	4.21917	Hydrophobic	Pi-Pi Stacked
	Isoorientin	−9.747	7.2	GLY143	2.8774	H-Bond	Conventional
				GLN189	3.18447	H-Bond	Pi-Donor
				GLN189	3.17864	H-Bond	H-Bond
				HIS41	4.97445	Hydrophobic	Pi-Donor
				HIS41	4.28696	Hydrophobic	H-Bond
							Pi-Pi T-shaped
							Pi-Pi T-shaped
	Myricetin	−9.252	6.8	ASN142	3.02118	H-Bond	Carbon H-Bond
				MET165	2.99789	H-Bond	Carbon H-Bond
	Isorhamnetin	−7.986	5.9	HIS41	3.06414	H-Bond	Conventional
				MET165	2.96127	H-Bond	Carbon H-Bond
	α-Ketoamide	−7.81	5.7	GLY143	2.57504	H-Bond	Conventional
				GLY143	2.48354	Hydrophobic	Conventional
				SER144	2.08599		Conventional
				SER144	2.12711		Conventional
				CYS145	2.67788		Conventional
				GLY143	2.536		Carbon H-Bond
				MET49	4.92426		Alkyl
RdRp	Cinnamtannin	−9.213	6.8	ARG555	1.91811	H-Bond	Conventional
				LYS798	4.5614	Hydrophobic	Alkyl
				TRP800	5.31303	Hydrophobic	Pi-Alkyl
	IsoSkimmiwallin	−9.12	6.7	LYS545	2.92032	H-Bond	Conventional
				ARG553	2.2876	H-Bond	Conventional
				ARG555	2.60482		Conventional
				ASP623	2.33349		Conventional
				THR687	3.06709		Conventional
				SER814	2.58688		Conventional
				SER814	2.42324		Carbon H-Bond
	Terflavin A	−9.813	7.2	LYS551	2.28502	H-Bond	Conventional
				ARG553	2.37388	H-Bond	Conventional
				ARG553	2.17502	H-Bond	Conventional
				ARG553	2.24901	H-Bond	Conventional
				ARG555	2.1431	H-Bond	Conventional
				ARG555	2.33079		Conventional
				TRP800	2.45817		Conventional
				SER814	2.89635		Conventional
				LYS798	3.07905		Carbon H-Bond
				TRP800	2.78817		Carbon H-Bond
	Terchebulin	−9.721	7.1	ARG836	2.48144	H-Bond	Conventional
				GLY590	2.84809	H-Bond	Carbon H-Bond
				ARG836	2.44829	H-Bond	Carbon H-Bond
	Terflavin C	−9.21	6.8	ARG553	2.30084	H-Bond	Conventional
				TYR619	2.32115	H-Bond	Conventional
				TRP800	2.60237	H-Bond	Conventional
				ASP618	2.88372	H-Bond	Carbon H-Bond
				LYS621	2.47666	H-Bond	Carbon H-Bond
				CYS813	2.63729	H-Bond	Carbon H-Bond
	Remdesivir	−6.51	4.8	TYR619	2.56877	H-Bond	Conventional
				TRP800	2.14254	H-Bond	Conventional
				CYS813	2.95124	H-Bond	Conventional
				SER814	2.14804	H-Bond	Conventional
				LYS551	4.21273	Electrostatic	Pi-Cation

Table 2. The greater force and work value suggest strong binding of ligands to respective proteins [46].

Notably, the control drug α-Ketoamide asserts the highest force value 4807.6 pN, but it exhibits less work (452.4 kcal/mol) than Isoorientin which manifests the second-highest force (3201.6 pN) and highest work 591.3 kcal/mol among all 5 ligands while pulling away from Mpro protein. The isoquercitine exerts 2965.8 pN force and the second-highest work is 531.2 kcal/mol when pulling away from Mpro protein. The other 3 Ligands Arborside, Myricetin, and Isorhamnetin exhibit lower force and work when pulling away from Mpro when compared to the Isoorientin and Isoquercitine. These results strongly suggest that Isoquercitine and Isoorientin can be potent inhibitors of Mpro. In the cases of RdRp, IsoSkimmiwallin demonstrates ~7 times the highest force (3964.0 pN) and ~1.5 times higher work (716.6 kcal/mol) when compared to the control drug (Remdesivir) which displays 555.0 pN force and 111.3 kcal/mol work respectively. Terflavin A exhibits the second-highest force (1858.1 pN) but Terchebulin displays the second highest work (531.1 kcal/mol) done in terms of ligand pulling. The

Table 2
The force and work done calculated for 5 potent phytochemicals along with control against RdRp and Mpro using SMD simulation.

Protein	Drug	F_{max} (pN)	W_{max} (kcal/mol)
Mpro	Isoquercitine	2965.8	531.2
	Arborside	2710.1	296.1
	Isoorientin	3201.6	591.3
	Myricetin	2384.2	317.4
	Isorhamnetin	2590.7	297.2
	α-Ketoamide	4807.6	452.4
RdRp	Cinnamtannin	1194.3	487.2
	IsoSkimmiwallin	3964.0	716.6
	Terflavin A	1858.1	505.9
	Terchebulin	1669.3	531.1
	Terflavin C	1513.1	428.4
	Remdesivir	555.0	111.3

forces for Terchebulin and Terflavin C against RdRp are close to each other, whereas Cinnamtannin denotes the lowest force (1194.3 pN) when compared to 5 selected ligands but it was a bit higher than the control one (Remdesivir). Cinnamtannin, Terflavin A, and Terflavin C illustrate lower work as compared to IsoSkimmiwallin and Terchebulin (Table 2). The data displays that all five drugs against RdRp assert excellent binding forces as compared to the control drug Remdesivir. The overall result suggests that IsoSkimmiwallin and Terflavin A can be good inhibitors candidates against RdRp and therefore needs further investigations.

Force vs. Time and Force vs. Distance graphs For RdRp and Mpro have been displayed in Fig. 1. The force is increasing gradually with respect to time and distance. At a certain point, the value reaches a maximum level which is termed rupture force, after this point the force value is dropping gradually (Fig. 1A). The control drug (α-Ketoamide) shows the highest rupture force around 120ps whereas Isoorientin and Isoquercitine exhibit the rupture forces of around 25ps and 101ps, respectively. After showing rupture force at 85ps, the force value for Arborside remains constant till the end of the simulation. Myricetin and Isorhamnetin exhibit rupture forces at 120ps and 152ps, respectively, then their forces are reduced gradually. But at 138ps and 157ps the forces of Myricetin and Isorhamnetin increase suddenly. A similar pattern has been observed in the case of α-Ketoamide where at 128ps the force increased suddenly. Occasionally, the force can be increased due to a small fragment, at a certain time point after the ligand has no non-bonded interaction with protein. This may be happened because of solvation friction. However, such kind of increase is small which can be overlooked. The force vs. Distance graph for Mpro (Fig. 1B) displays a similar unique pattern as shown in Fig. 1A.

From Fig. 1C and D, it can be clearly seen that forces of all ligands are increasing and at certain points, it gets constant by forming a zigzag pattern graph till the forces reached rupture force point. After dissociation at rupture point, the forces are decreasing and the graph shows a zigzag pattern. However, the force increases suddenly after 60ps in the case of IsoSkimmiwallin despite the ligand being fully dissociated from RdRp protein and solvated totally. This seems to be because of solvent friction which can be ignored. The force vs. Distance graph for RdRp also exhibits a similar pattern as the Force vs. Time graph of RdRp. Herein,

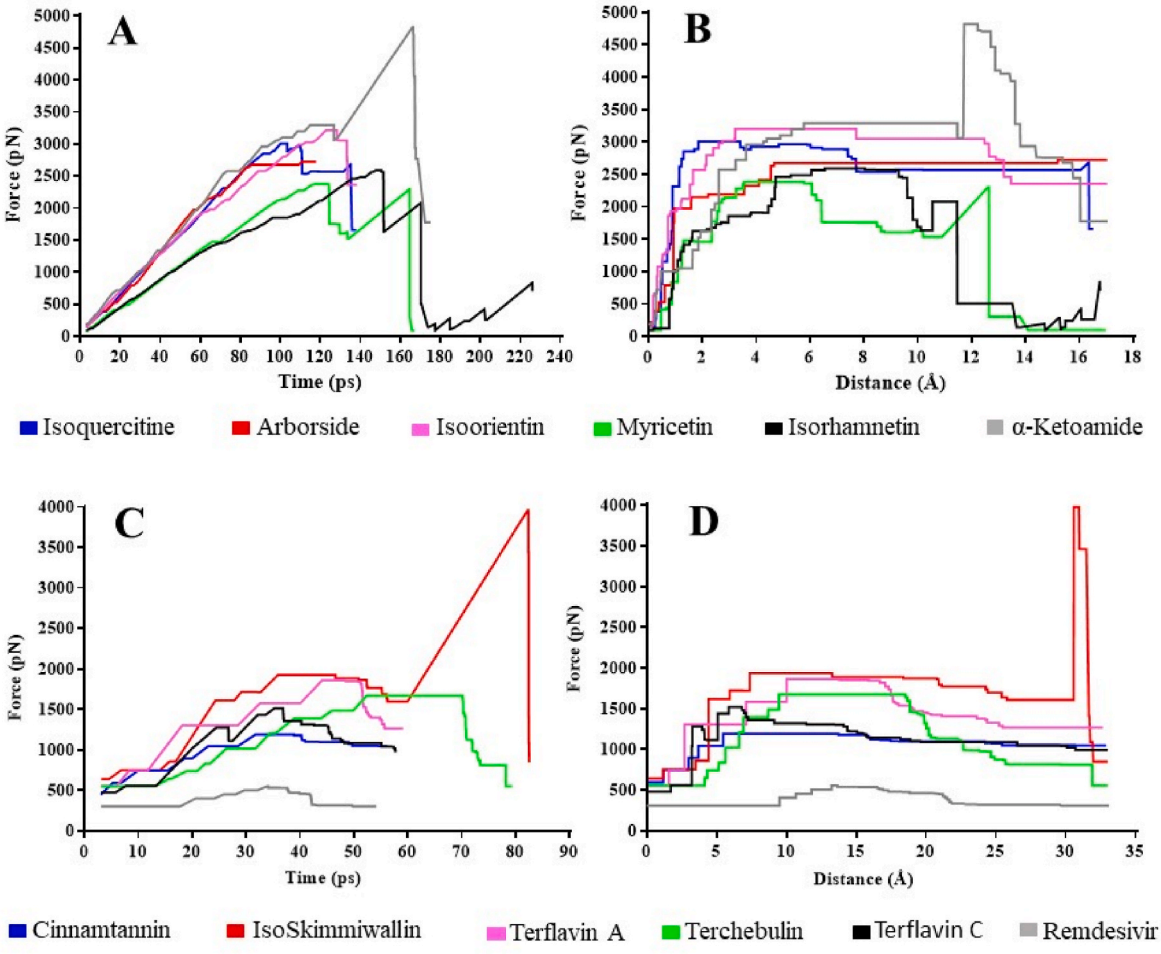

Fig. 1. Steered Molecular Dynamics simulations of 6 ligands. A) and B) Force vs. Time graph and Force vs. Distance graph, respectively, against Mpro; C) and D) Force vs. Time graph and Force vs. Distance graph, respectively, against RdRp.

initially, forces of all ligands have been increasing following the zigzag pattern with respect to distance followed by a decrease in force when ligands get dissociated.

Overall results indicate that Isoquercitine and Isoorientin for Mpro and IsoSkimmiwallin and Terflavin A for RdRp can be potential inhibitors. Therefore, these ligands are chosen for further investigations. Structural representation for Isoquercitine, Isoorientin of Mpro and IsoSkimmiwallin, Terflavin A of RdRp in SMD is illustrated in Fig. 2.

3.3. Molecular dynamics simulations

Molecular dynamics simulation was carried out for the apo and four promising complexes (which shows the highest force and work in steered molecular dynamics simulations) of Mpro and RdRp respectively. The alpha ketoamide (Ak) and remdesivir are taken as control drugs for Mpro and RdRp protein respectively. RMSD of the protein backbone, RMSF, Rg, and SASA was calculated.

The lower RMSD value of the protein backbone denotes the high stability of the protein-ligand complex. In the case of simulations against Mpro, AK-Mpro (Dark Midnight Blue curve) complex fluctuates with RMSD around 1–3 Å, on the other hand, apo-Mpro (Tyrian purple curve) was static over the simulation period. However, the last 20 ns RMSD of AK-Mpro was observed quite similar to the apo-Mpro in Fig. 3A. Isoorientin-Mpro complex (Brass green curve) shows similar RMSD (2–3.3 Å) when compared with AK-Mpro and apo-Mpro over 200 ns which indicates that isoorientin is bound stably to the protein during the whole simulation. Over the simulation, isoquercitine gets detached in remarkable time points from Mpro protein while isoorientin shows no deviation from the binding pocket of Mpro as revealed by snapshots (Fig. 5). In the case of RDRP, the RMSD of apo-RdRp (Tyrian purple curve) was quite unstable after around 120ns and in the case of isoskimmiwallin-RdRp (Robin's Egg Blue curve), the RMSD was increased to 9 Å at 35 ns and then declined to around 7 Å for the last 160 ns. Also, the last RMSD peak was similar for both cases which suggest that the fluctuation could be due to the instability of the RdRp in physiological conditions. When MD snapshots were analyzed, it became clear that such changes in rmsd were not due to the movement of the ligand, rather it could be attributed to the change in RdRp protein conformation (Fig. 6A). The RMSD of terflavin A-RdRp (Brass green curve) and remdesivir-RdRp (Dark Midnight Blue curve) were quite similar (around 2 Å) throughout the simulation; indicating that the trajectories generated during the whole run are more stable than apo-RdRp (Fig. 3A) and snapshots also showing stability in case of terflavin A-RdRp (Fig. 6B).

RMSF (root mean square fluctuations) calculation shows higher fluctuation for isoorientin-Mpro than isoquercitine-Mpro and apo-Mpro while AK-Mpro shows the lowest fluctuations over the whole time which is presented in Fig. 3B. For isoquercitine-Mpro and AK-Mpro, residues of 100–200 regions' fluctuation patterns are almost overlapping, in contrast, these regions' fluctuation patterns are distinct from apo-Mpro. The residues of around 300 regions show significant fluctuation for isoorientin-Mpro compared to other complexes. On the other hand, the greatest fluctuations were observed, almost 32 Å, for isoskimmiwallin-RdRp and apo-RdRp from 69 to 74 regions, then, the fluctuations dramatically fall to 5 Å. In between 75 and 932 regions, there are no significant fluctuations for all the complexes including apo-RdRp as

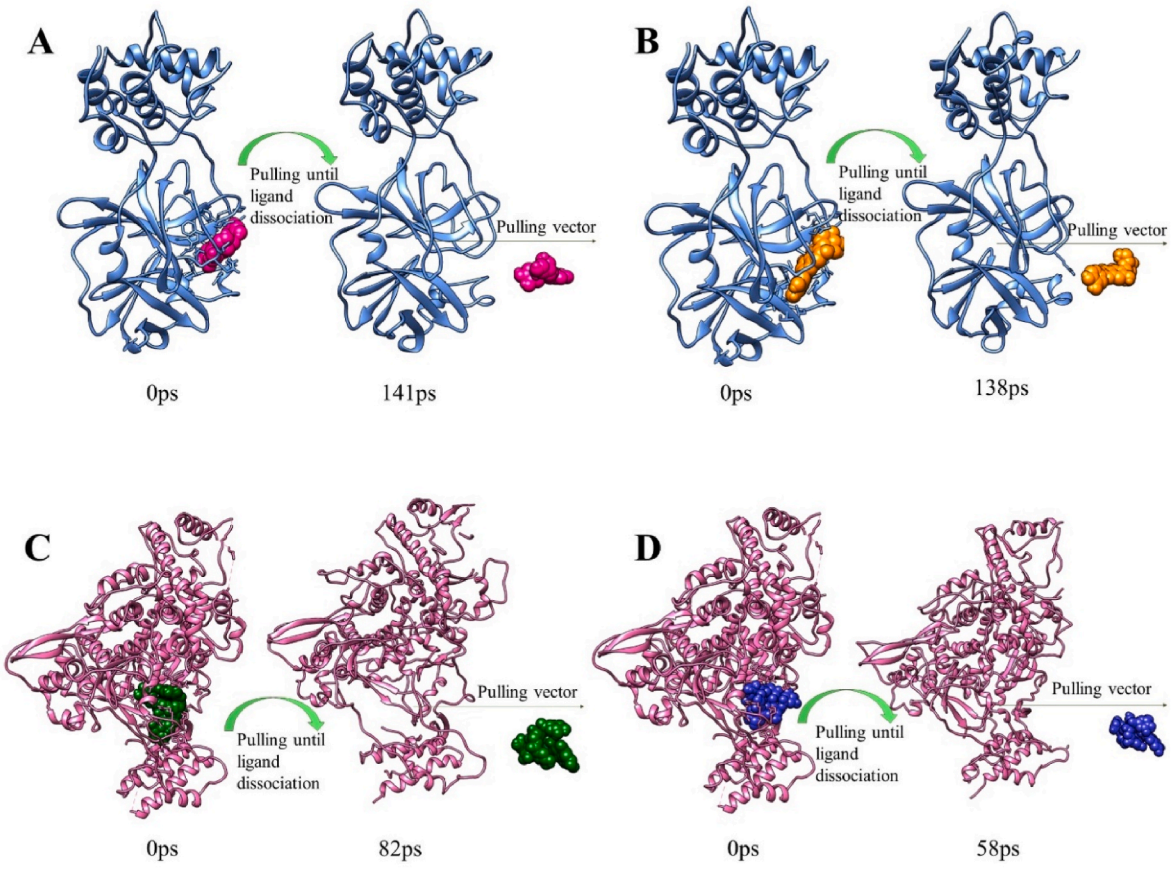

Fig. 2. Structural representations of 2 best ligands against 2 proteins in Steered Molecular Dynamic simulations before and after dissociation. A) Isoquercitine-Mpro complex (Isoquercitine-deep pink, Mpro- sky blue); B) Isoorientin-Mpro complex (Isoorientin- orange); C) IsoSkimmiwallin-RdRp complex (IsoSkimmiwallin- deep green, RdRp - hot pink); D) Terflavin A-RdRp complex (Terflavin A- blue). (For interpretation of the references to colour in this figure legend, the reader is referred to the Web version of this article.)

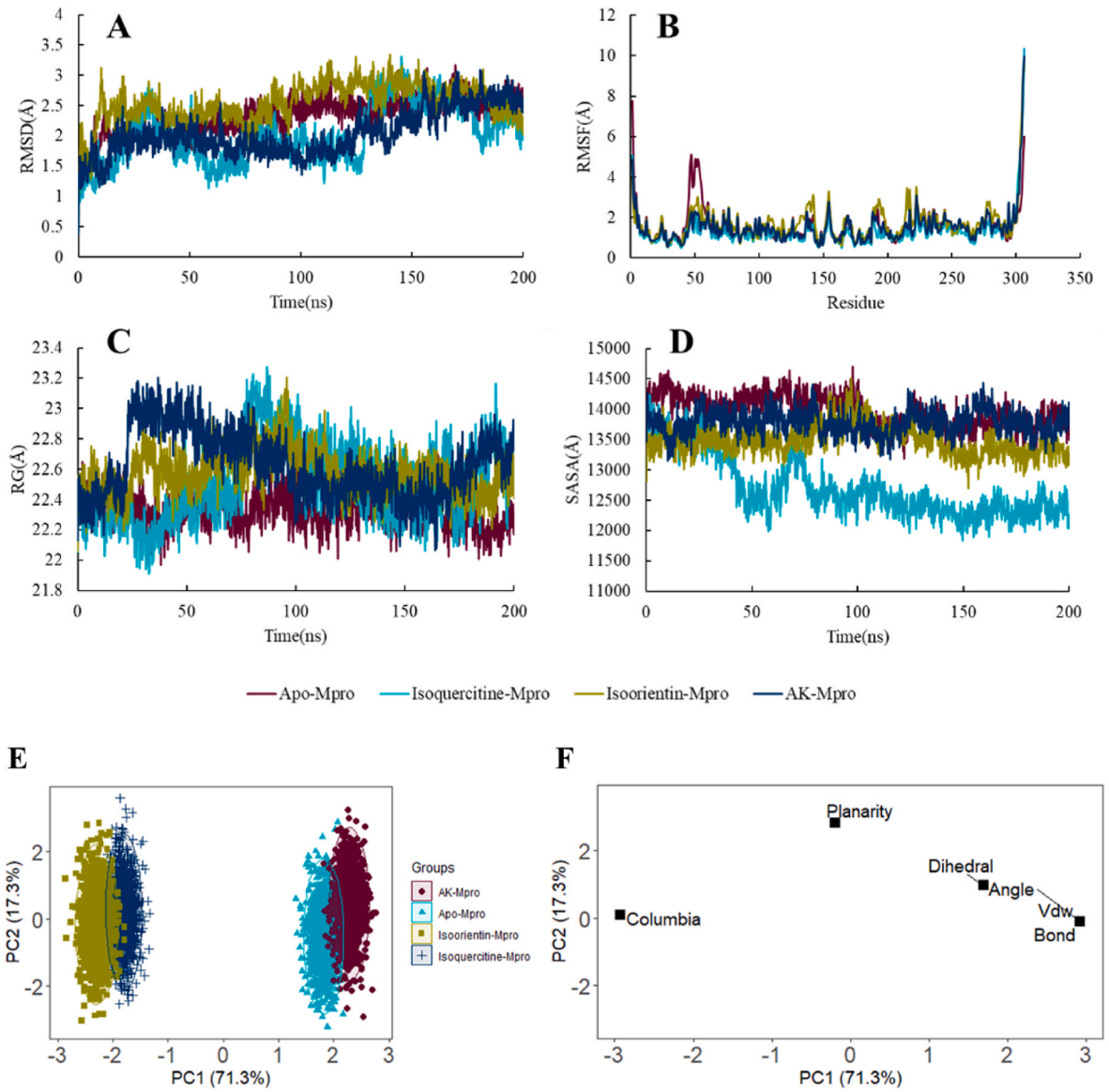

Fig. 3. (A) RMSD, (B) RMSF, (C) Radius of gyration (Rg), (D) SASA, (E) Score plot, and (F) Loading plot of Apo-Mpro and ligand−Mpro complexes over 200 ns MD simulation time.

shown in Fig. 4B. These fluctuations for both isoskimmiwallin-RdRp and apo-RdRp from 69 to 74 regions could be responsible for the high RMSD of these complexes. Moreover, it indicates the conformational changes in protein structure under the physiological condition which could be a barrier to ligand activity.

To investigate the structural compactness and solvent accessibility of all complexes we observe the radius of gyration (Rg) and solvent accessible surface area (SASA). The radius of gyration is stated as the distance from an axis at which the mass of a body may be assumed to be concentrated. The radius of gyrationat is found 22–22.7 Å for apo-form of Mpro which indicates that the apoprotein is almost stable during the whole run. For both ligands complex the Rg fluctuates for the first 100 ns, then it was quite stable. AK-Mpro was unstable over time in comparison to others (Fig. 3C). On the other hand, the Rg of remdesivir-RdRp was quite stable over the simulation period and the terflavin A-RdRp complex (average 30.3 Å) shows a similar pattern as well (Fig. 4C). The apo-RdRp and isoskimmiwallin-RdRp display significant fluctuation over time and the last peak were similar. This result also supports the RMSD fluctuation of both complexes.

Besides, Solvent accessible surface area (SASA) of proteins has always been considered a decisive factor in protein folding and stability studies. It is defined as the surface characterized around a protein by a hypothetical center of a solvent sphere with the Van der Waals contact surface of the molecule. Isoquercitine-Mpro complex depicts the lowest value (below 13,000 Å2) of SASA as compared to apo-Mpro and other complexes as illustrated in Fig. 3D. The case of apo-RdRp exhibits a high SASA value as compared to others (Fig. 4D). The SASA value of the isoskimmiwallin-RdRp was similar to apo after 120 ns. The lowest value was observed in the case of remdesivir-RdRp and also a similar value was noticed for terflavin A-RdRp after 130ns.

During MD simulation, a PCA model is generated to understand structural and energy changes in the ligand−protein complexes relative to apo-protein. In Fig. 3, the PCA model consists of four training sets (Apo-Mpro and three ligand−Mpro complexes), and the PCA model shown in Fig. 4 consists of four training sets (Apo-RdRp and three ligand−RDRP complexes). Here, column energy, angle, bond distance, dihedral, planarity, and VdW energies are considered as variables.

For the PCA model (Figs. 3E), 88.6% of the variance is explained by the first two PCs, where PC1 describes 71.3% and PC2 denotes 17.3% of the variance. The PC1 and PC2 plots show AK-Mpro and apo-Mpro

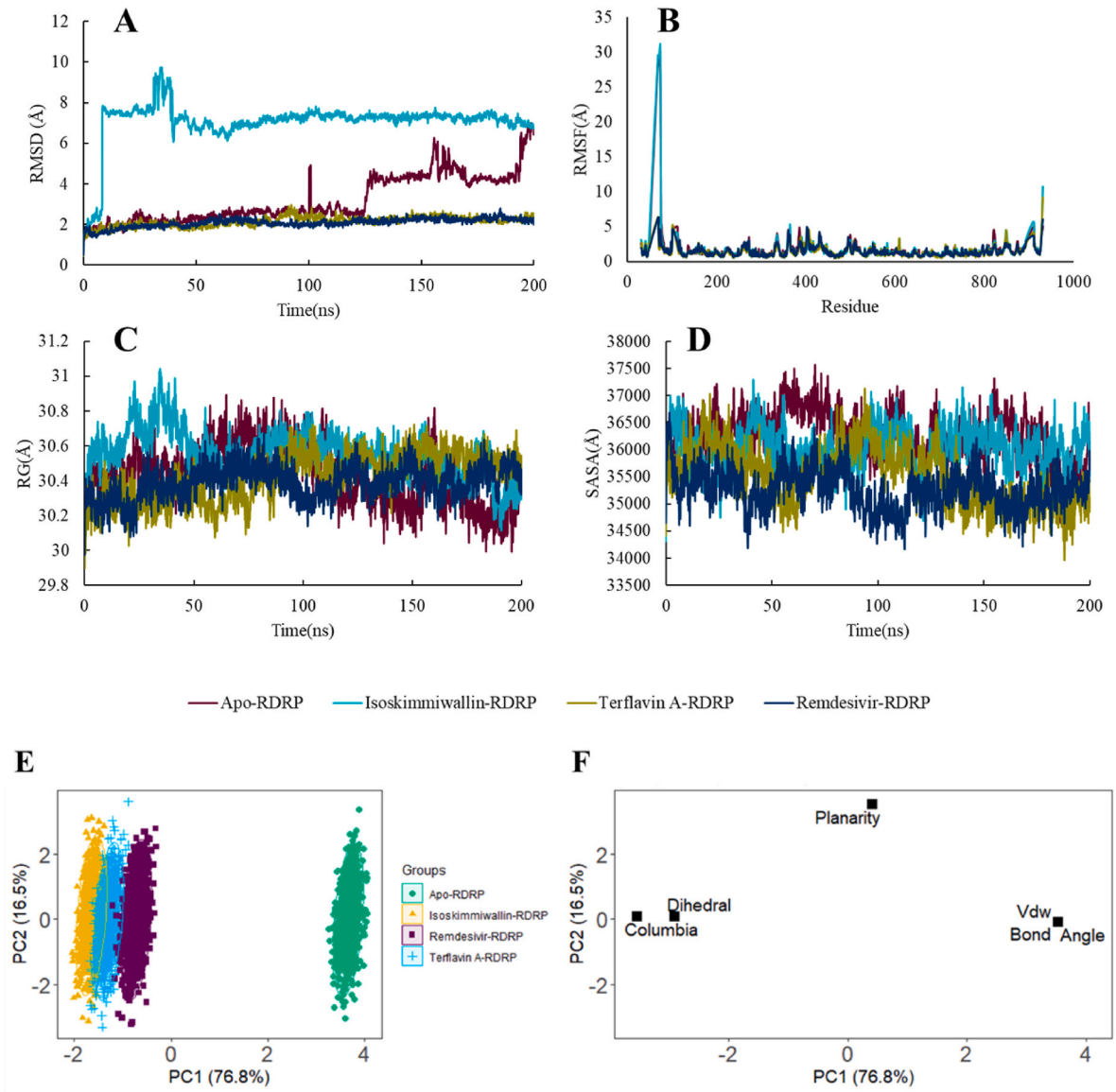

Fig. 4. (A) RMSD, (B) RMSF, (C) Radius of gyration (Rg), (D) SASA, (E) Score plot, and (F) Loading plot of Apo-RdRp and ligand−RDRP complexes over 200 ns MD simulation time.

exhibit approximately similar patterns, on the other hand, isoquercitine-Mpro, and isoorientin-Mpro show similar patterns. In the loading plot (Fig. 3F) dihedral, angle, VdW, and bond positively correlate with apo-Mpro and AK-Mpro. In contrast, coloumb negatively correlates with isoquercitine-Mpro, and isoorientin-Mpro. The coloumb and planarity could be the shifting reasons for the complexes.

For the RdRp PCA, in Fig. 4E, PC1, and PC2 explain 93.3% of the variance. Where 76.8% and 16.5% of the variance is denoted by PC1 and PC2 respectively. As shown in Fig. 4E, the PC1 and PC2 revealed that isoskimmiwallin-RdRp, remdesivir-RdRp, and terflavin A-RdRp resided nearly in contrast to the apo-RdRp. The overlapping PCA plot of remdesivir-RdRp, and terflavin A- RdRp supports the RMSD. In the loading plot (Fig. 4F) angle, VdW, and bond positively correlate with apo- RdRp. In contrast coloumb, dihedral negatively correlates with isoskimmiwallin- RdRp, remdesivir- RdRp, and terflavin A- RdRp. Coloumb, dihedral, and planarity could be the shifting reasons for the ligand complexes from apo RdRp.

Hydrogen bonding played a crucial role in ligand− RdRp interaction, contributing 99% of all interactions while hydrophobic and electrostatic interactions contributed only 1% of the total interactions. Various amino acid residues including LYS773, Ser814, Arg836, ASP760, ASP761, TYR619, ASP623, and GLU811 present in the binding site of the RdRp were involved in noncovalent interactions with the ligands (Figs. 6 and 7). In the case of ligand−Mpro complexes, isoquercitine-Mpro depicts a 75% hydrogen bond while isoorientin-Mpro shows a 66% hydrogen bond. Some active residues such as His41, Cys145, Hip164, Met165, Glu166, Arg188, Gln189, VAL186, and Thr190 of Mpro interact most frequently with the ligands (Fig. 8).

Moreover, terflavin A-RdRp and isoorientin-Mpro remained stable in the entire molecular dynamic simulation. Therefore, it can be articulated that isoorientin and terflavin A can be considered better drugs to inhibit the Mpro and RdRp protein of SARS CoV 2 respectively when compared to the control drug.

4. Discussion

Molecular docking-based virtual screening methods have several advantages over traditional approaches for searching therapeutic molecules for drug re-purposing. Given the stringent situation, these methods could offer a fast, reliable, and cost-effective way of identifying

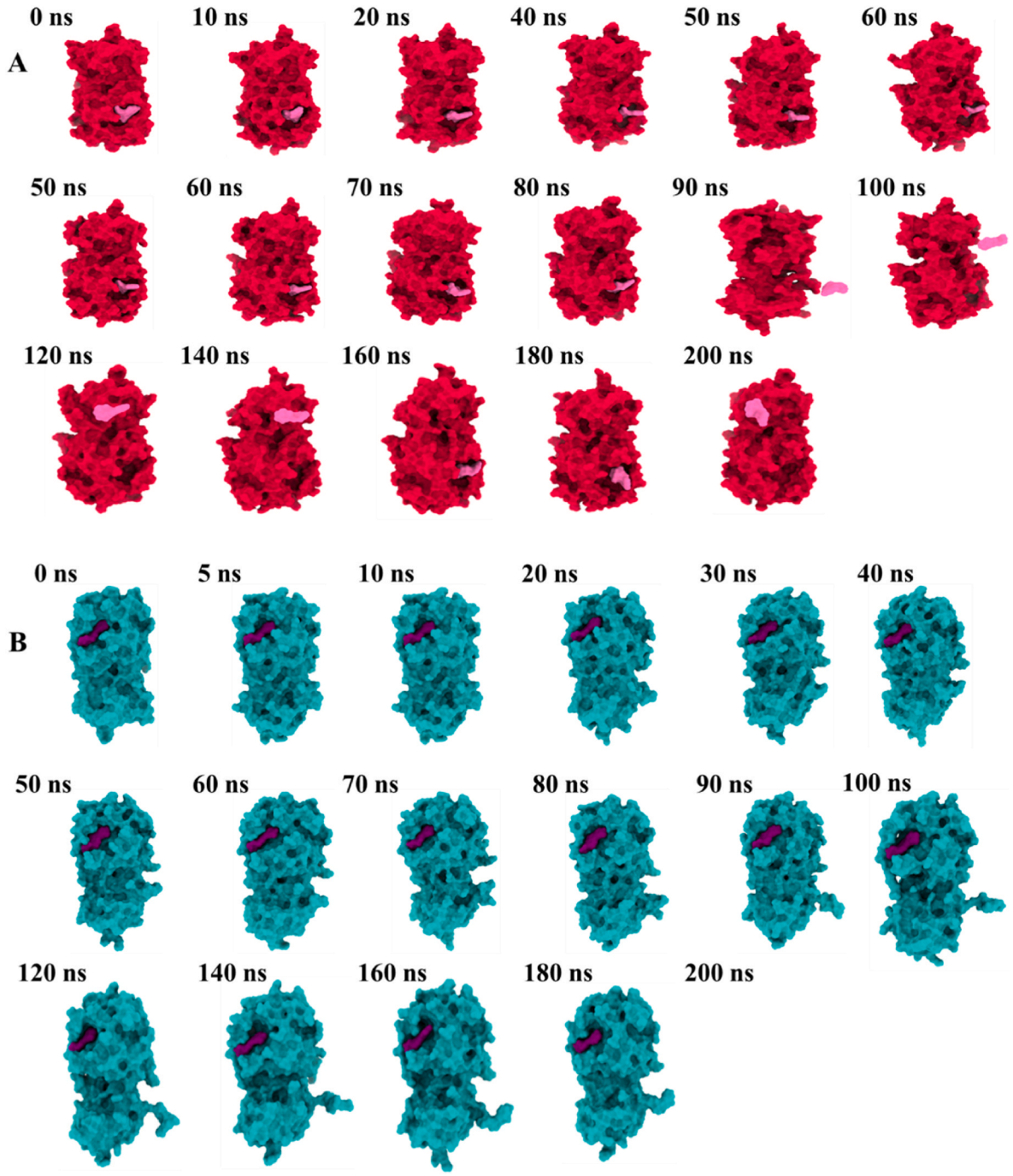

Fig. 5. Representative snapshots (A) Isoquercitine-Mpro, (B) Isoorientin-Mpro throughout 200 ns simulations.

therapeutic drugs. In recent times, phytochemical-based drug repurposing has shown greater potential owing to fewer side effects and comparable therapeutic efficacy in a cost-effective manner [18–22]. Several studies have examined the therapeutic value of phytochemicals for the treatment of SARS-CoV-2 protein targets, mainly RdRp and Mpro, which may play a role in conferring protection against severe COVID-19 infection [17,23,47]. Our study extended this knowledge through virtual screening of 1064 phytochemicals against RdRp and Mpro using molecular docking approaches. The findings suggested that the selected molecules have therapeutic potential and can therefore be used as a preventive measure in fatal COVID-19 cases. Specifically, based on the binding interaction and affinities of the ligand with the catalytic site residues of the protein, we found that the ligands form stable complexes with target proteins, thereby potentially inhibiting viral growth. Cinnamtannin, isoskimmiwallin, terflavin A, terchebulin, and terflavin C showed high binding affinities to RdRp, whereas isoquercitin, arborside, isoorientin, myricetin, and isorhamnetin exhibited high docking scores for Mpro (Table 1). The ADMET profiles of the lead hit molecules were found to be more suitable than those of the control drugs, α-ketoamide, and remdesivir (Supplementary Table 1). Five potential compounds that showed high affinities after docking against each protein target were subjected to SMD simulations. Based on the calculations of force and work done to pull ligand molecules away from their respective protein targets, we selected the four best ligands against RdRp and Mpro (Table 2), which were further subjected to molecular dynamic simulation. In addition to these four ligands, remdesivir against RdRp and α-ketoamide against Mpro were used as controls.

Molecular dynamics simulation results suggested that remdesivir-

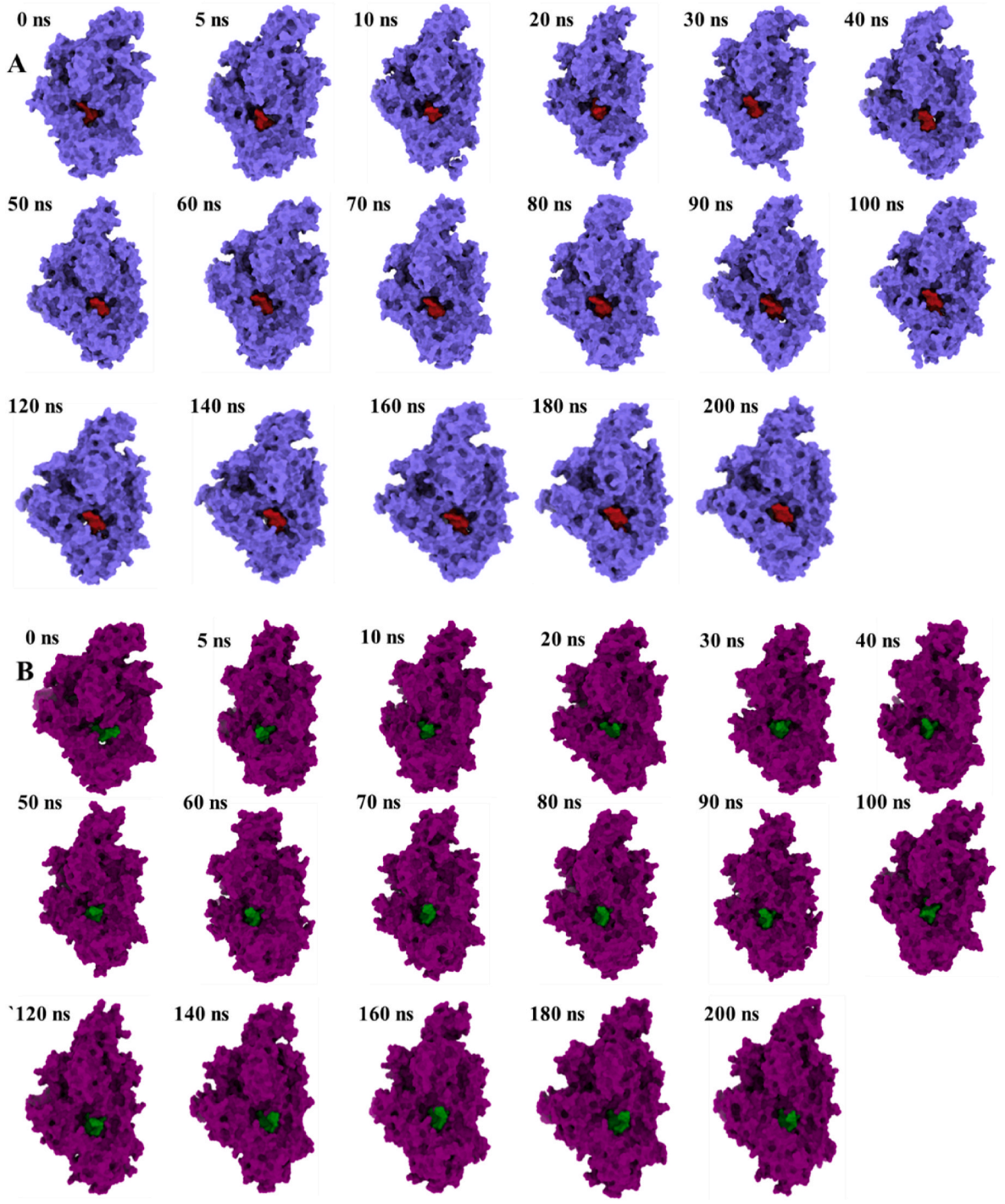

Fig. 6. Representative snapshots (A) Isoskimmiwallin-RdRp, (B) Terflavin A-RdRp throughout 200 ns simulations.

RdRp and α-ketoamide-Mpro complexes exhibited lower RMSD values than apo and isoskimmiwallin-RdRp, terflavin A-RdRp, isoquercitin-Mpro, and isoorientin-Mpro complexes, respectively, thereby indicating their higher stability throughout the 200 ns simulation. Additionally, the lower SASA values of the complexes further strengthened the conclusion that the binding of these ligands stabilizes RdRp and Mpro. Furthermore, the RMSF and Rg analyses of all complexes suggested the compactness of the protein structure after binding to the ligands. The top hits for RdRp were isoskimmiwallin and terflavin A. The study conducted by Puttaswamy et al. demonstrates the antiviral potential of terflavin in reducing SARS-CoV-2 pathogenesis [48]. Skimmiwallin and related compounds are known phytochemicals with therapeutic potential, but we did not find any reports describing the inhibitory potential of isoskimmiwallin against SARS-CoV-2 RdRp. A recent study by Yalcin et al. shows the antiviral potential of isoorientin, luteolin, lucenin, oleanolic acid, isochaphoside, saponarin, and schaftoside against Mpro [49–51]. Furthermore, several studies demonstrate the antiviral potential of quercetin, either alone [50] or in combination with vitamins C [51] and D [52]. The evidence presented by Biancatelli et al. (2020) regarding the use of vitamin C and quercetin as prophylactic therapeutic agents in high-risk populations and for the treatment of COVID-19 patients supports the use of phytochemicals [51]. Another proof-of-concept study, which is currently under clinical trial, demonstrates that quercetin/vitamin D/estradiol may affect the expressions of

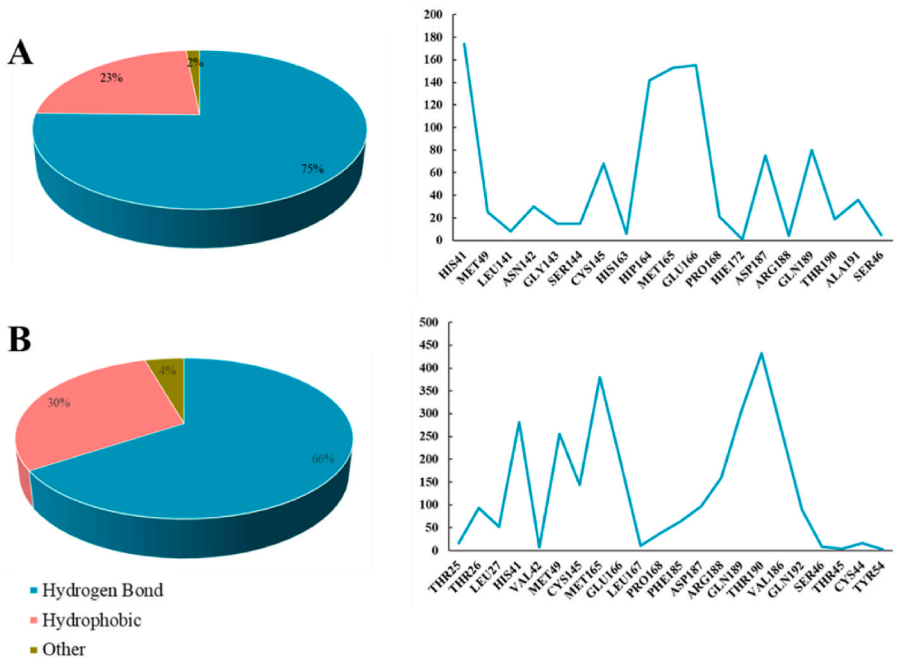

Fig. 7. Distribution of noncovalent interactions, and interacting residues of the (A) Isoskimmiwallin−RDRP and (B) Terflavin A−RDRP over 200 ns MD simulation time.

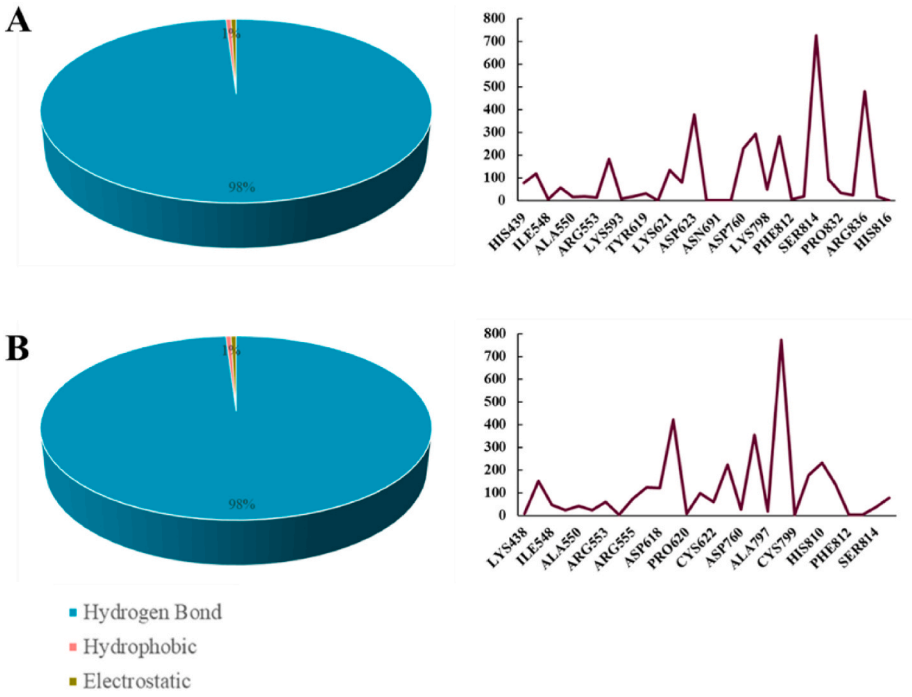

Fig. 8. Distribution of noncovalent interactions, and interacting residues of the (A) Isoquercitine-Mpro, and (B) Isoorientin-Mpro over 200 ns MD simulation time.

244 out of 332 (73%) human genes encoding SARS-CoV-2 targets [52]. We had included quercetin in our *in silico* screening library; however, we did not find a higher affinity or inhibitory potential of quercetin against Mpro relative to Iso quercetin, and this needs to be investigated further.

The MM/PBSA calculations suggested that the binding free energies of all four complexes were the lowest for the most part during the simulation. In addition, PCA analysis revealed that terflavin A-RdRp and isoorientin-Mpro were the best ligands that stabilized RdRp and Mpro relative to the control, consistent with the RMSF, Rg, and SASA analyses.

From the binding frequency data, active site information for Mpro-ligand complexes over the simulation time showed a similar catalytic dyad of His41 and Cys145 [52], which has been reported previously [53–55]. Furthermore, the active site observations for RdRp were supported by other researchers such as Aftab et al., who report that ASP760 and ASP761 can be potential binding sites [56,57].

Moreover, terflavin A-RdRp and isoorientin-Mpro remained stable throughout the molecular dynamics simulation. Therefore, isoorientin and terflavin A can be used as potential drugs to inhibit the Mpro and RdRp proteins of SARS CoV 2, respectively, as compared to the control drug. *In silico* studies have added advantages in terms of rapid drug

discovery and understanding the molecular dynamic profiles of drugs inside the binding pocket. However, further *in vitro* and *in vivo* examinations are warranted to understand the behavioral kinetics of drugs inside living systems.

5. Conclusion

In this study, we focused on the virtual screening of phytochemical molecules with inhibitory potential against two main targets (RdRp and Mpro) of SARS-CoV-2 using molecular docking and molecular dynamics simulation approaches. Among the leads screened from 1064 molecules, isoskimmiwallin and terflavin A exhibited strong binding forces against RdRp, whereas isoquercitin and isoorientin demonstrated high binding forces against Mpro. Furthermore, the work done to pull away from these ligands from their respective protein targets was substantially more than that of the control drugs, thereby suggesting their higher inhibitory potentials. Moreover, these molecules also formed stable complexes with their respective protein targets and exhibited higher binding energies. Thus, our results demonstrated that isoskimmiwallin, terflavin A, isoquercitin, and isoorientin possess high inhibitory potential against the main targets of SARS-CoV-2 and warrant further *in vitro* and *in vivo* evaluation.

Declarations

We confirm that this manuscript is an original work and is not under consideration by any journal.

Ethics approval and consent to participate

Not applicable.

Human and animal rights

No humans/animals were used in the study that is the base of this research.

Consent for publication

Not applicable.

Availability of data and materials

All data generated or analyzed during this study are included in this published article.

Code availability

Not applicable.

Funding

None.

Declaration of competing interest

The authors declare no conflict of interest, financial or otherwise.

Acknowledgment

All authors are thankful to Mohammad A Halim for his kind suggestion and guidance throughout the research work. Also, we are grateful to The Red-Green Research Center, Bangladesh for providing us High-Performance Computer facility for performing molecular dynamics simulation. The authors would like to thank team Schrodinger for providing the software evaluation version. Arpana Parihar is thankful to DST for providing fellowship under DST-WoS-B Scheme. The calculation of work done by Suprio is duly acknowledged.

Appendix A. Supplementary data

Supplementary data to this article can be found online at https://doi.org/10.1016/j.compbiomed.2022.105468.

References

[1] Coronavirus Disease, COVID-19) Situation Reports, n.d. https://www.who.int/emergencies/diseases/novel-coronavirus-2019/situation-reports. (Accessed 5 February 2022).
[2] W. Wang, J. Tang, F. Wei, Updated understanding of the outbreak of 2019 novel coronavirus (2019-nCoV) in Wuhan, China, J. Med. Virol. 92 (2020) 441–447, https://doi.org/10.1002/JMV.25689.
[3] R. Yan, Y. Zhang, Y. Li, L. Xia, Y. Guo, Q. Zhou, Structural basis for the recognition of SARS-CoV-2 by full-length human ACE2, Science 367 (2020) 1444–1448, https://doi.org/10.1126/SCIENCE.ABB2762/SUPPL_FILE/ABB2762S1.MP4.
[4] A. Parihar, P. Ranjan, S.K. Sanghi, A.K. Srivastava, R. Khan, Point-of-Care biosensor-based diagnosis of COVID-19 holds promise to combat current and future pandemics, ACS Appl. Bio Mater. 3 (2020) 7326–7343, https://doi.org/10.1021/ACSABM.0C01083.
[5] J. Lan, J. Ge, J. Yu, S. Shan, H. Zhou, S. Fan, Q. Zhang, X. Shi, Q. Wang, L. Zhang, X. Wang, Structure of the SARS-CoV-2 spike receptor-binding domain bound to the ACE2 receptor, Nature 581 (2020) 215–220, https://doi.org/10.1038/s41586-020-2180-5, 7807. 581 (2020).
[6] E. Andreano, R. Rappuoli, SARS-CoV-2 escaped natural immunity, raising questions about vaccines and therapies, Nat. Med. 27 (5) (2021) 759–761, https://doi.org/10.1038/s41591-021-01347-0, 27 (2021).
[7] D. van Egeren, A. Novokhodko, M. Stoddard, U. Tran, B. Zetter, M. Rogers, B. L. Pentelute, J.M. Carlson, M. Hixon, D. Joseph-McCarthy, A. Chakravarty, Risk of rapid evolutionary escape from biomedical interventions targeting SARS-CoV-2 spike protein, PLoS One 16 (2021), e0250780, https://doi.org/10.1371/JOURNAL.PONE.0250780.
[8] A. Khan, T. Zia, M. Suleman, T. Khan, S.S. Ali, A.A. Abbasi, A. Mohammad, D. Q. Wei, Higher infectivity of the SARS-CoV-2 new variants is associated with K417N/T, E484K, and N501Y mutants: an insight from structural data, J. Cell. Physiol. 236 (2021) 7045–7057, https://doi.org/10.1002/JCP.30367.
[9] M.T. Khan, M.J. Islam, A. Parihar, R. Islam, T.J. Jerin, R. Dhote, M.A. Ali, F. K. Laura, M.A. Halim, Immunoinformatics and molecular modeling approach to design universal multi-epitope vaccine for SARS-CoV-2, Inform. Med. Unlocked 24 (2021), 100578, https://doi.org/10.1016/J.IMU.2021.100578.
[10] K.T. Choy, A.Y.L. Wong, P. Kaewpreedee, S.F. Sia, D. Chen, K.P.Y. Hui, D.K.W. Chu, M.C.W. Chan, P.P.H. Cheung, X. Huang, M. Peiris, H.L. Yen, Remdesivir, lopinavir, emetine, and homoharringtonine inhibit SARS-CoV-2 replication in vitro, Antivir. Res. 178 (2020), 104786, https://doi.org/10.1016/J.ANTIVIRAL.2020.104786.
[11] H. Li, Z. Liu, J. Ge, Scientific research progress of COVID-19/SARS-CoV-2 in the first five months, J. Cell Mol. Med. 24 (2020) 6558–6570, https://doi.org/10.1111/JCMM.15364.
[12] J. Santos, S. Brierley, M.J. Gandhi, M.A. Cohen, P.C. Moschella, A.B.L. Declan, Repurposing therapeutics for potential treatment of SARS-CoV-2: a review, Viruses 12 (2020) 705, https://doi.org/10.3390/V12070705, 12 (2020) 705.
[13] E.R. Fox, M. Shah, R. Vinik, S. Brown, W. Buckel, B. Webb, J. Zarndt, M. Evans, P. Mesdaghi, H.N. Imlay, E.S. Spivak, Developing statewide remdesivir use criteria, Am. J. Health Syst. Pharm. 78 (2021) 732–735, https://doi.org/10.1093/AJHP/ZXAB009.
[14] A. Elbeddini, C.X. Wen, Y. Tayefehchamani, A. To, Mental health issues impacting pharmacists during COVID-19, J. Pharm. Pol. Pract. 13 (2020) 1–6, https://doi.org/10.1186/S40545-020-00252-0/FIGURES/1.
[15] A. Parihar, T. Zafar, R. Khandia, D. Singh, P. Barkatullah, R. Dhote, Y. Mishra, In Silico Analysis for the Repurposing of Broad-Spectrum Antiviral Drugs against Multiple Targets from SARS-CoV-2: A Molecular Docking and ADMET Approach, 2022, https://doi.org/10.21203/rs.3.rs-1242644/v1.
[16] A. Sternberg, D.L. McKee, C. Naujokat, Novel drugs targeting the SARS-CoV-2/COVID-19 machinery, Curr. Top. Med. Chem. 20 (2020) 1423–1433, https://doi.org/10.2174/1568026620999200517043137.
[17] Z. Jin, H. Wang, Y. Duan, H. Yang, The main protease and RNA-dependent RNA polymerase are two prime targets for SARS-CoV-2, Biochem. Biophys. Res. Commun. 538 (2021) 63–71, https://doi.org/10.1016/J.BBRC.2020.10.091.
[18] B.G. Vijayakumar, D. Ramesh, A. Joji, J. Jayachandra prakasan, T. Kannan, In silico pharmacokinetic and molecular docking studies of natural flavonoids and synthetic indole chalcones against essential proteins of SARS-CoV-2, Eur. J. Pharmacol. 886 (2020) 173448, https://doi.org/10.1016/J.EJPHAR.2020.173448.
[19] P. Kar, V. Kumar, B. Vellingiri, A. Sen, N. Jaishee, A. Anandraj, H. Malhotra, S. Bhattacharyya, S. Mukhopadhyay, M. Kinoshita, V. Govindasamy, A. Roy, D. Naidoo, M.D. Subramaniam, Anisotine and Amarogentin as Promising Inhibitory Candidates against SARS-CoV-2 Proteins: a Computational Investigation, 2020, https://doi.org/10.1080/07391102.2020.1860133. Https://Doi.Org/10.1080/07391102.2020.1860133.
[20] R.S. Joshi, S.S. Jagdale, S.B. Bansode, S.S. Shankar, M.B. Tellis, V.K. Pandya, A. Chugh, A.P. Giri, M.J. Kulkarni, Discovery of potential multi-target-directed

ligands by targeting host-specific SARS-CoV-2 structurally conserved main protease, J. Biomol. Struct. Dyn. (2020) 1–16, https://doi.org/10.1080/07391102.2020.1760137/SUPPL_FILE/TBSD_A_1760137_SM3442.XLS.
[21] P. Kar, N.R. Sharma, B. Singh, A. Sen, A. Roy, Natural compounds from Clerodendrum spp. as possible therapeutic candidates against SARS-CoV-2: an in silico investigation, J. Biomol. Struct. Dyn. 39 (2021) 4774–4785, https://doi.org/10.1080/07391102.2020.1780947/SUPPL_FILE/TBSD_A_1780947_SM4552.DOCX.
[22] R. Islam, M.R. Parves, A.S. Paul, N. Uddin, M.S. Rahman, A. al Mamun, M. N. Hossain, M.A. Ali, M.A. Halim, A molecular modeling approach to identify effective antiviral phytochemicals against the main protease of SARS-CoV-2, J. Biomol. Struct. Dyn. 39 (2021) 3213–3224, https://doi.org/10.1080/07391102.2020.1761883/SUPPL_FILE/TBSD_A_1761883_SM6768.DOCX.
[23] M. Kandeel, Y. Kitade, A. Almubarak, Repurposing FDA-approved phytomedicines, natural products, antivirals and cell protectives against SARS-CoV-2 (COVID-19) RNA-dependent RNA polymerase, PeerJ 8 (2020), e10480, https://doi.org/10.7717/PEERJ.10480/SUPP-13.
[24] G. Madhavi Sastry, M. Adzhigirey, T. Day, R. Annabhimoju, W. Sherman, Protein and ligand preparation: parameters, protocols, and influence on virtual screening enrichments, J. Comput. Aided Mol. Des. 27 (2013) 221–234, https://doi.org/10.1007/s10822-013-9644-8.
[25] D.C. Bas, D.M. Rogers, J.H. Jensen, Very fast prediction and rationalization of pKa values for protein–ligand complexes, Proteins: Struct. Funct. Bioinform. 73 (2008) 765–783, https://doi.org/10.1002/PROT.22102.
[26] W.L. Jorgensen, J. Tirado-Rives, The OPLS [optimized potentials for liquid simulations] potential functions for proteins, energy minimizations for crystals of cyclic peptides and crambin, J. Am. Chem. Soc. 110 (1988) 1657–1666, https://doi.org/10.1021/JA00214A001.
[27] S. Ahmed, R. Mahtarin, M.S. Islam, S. Das, A. al Mamun, S.S. Ahmed, M.A. Ali, Remdesivir analogs against SARS-CoV-2 RNA-dependent RNA polymerase, J. Biomol. Struct. Dynam. (2021), https://doi.org/10.1080/07391102.2021.1955743.
[28] S. Bhowmick, A. Saha, S.M. Osman, F.A. Alasmary, T.M. Almutairi, M.A. Islam, Structure-based identification of SARS-CoV-2 main protease inhibitors from anti-viral specific chemical libraries: an exhaustive computational screening approach, Mol. Divers. 25 (2021), https://doi.org/10.1007/S11030-021-10214-6/TABLES/5, 1979–1997.
[29] S. Kim, J. Chen, T. Cheng, A. Gindulyte, J. He, S. He, Q. Li, B.A. Shoemaker, P. A. Thiessen, B. Yu, L. Zaslavsky, J. Zhang, E.E. Bolton, PubChem 2019 update: improved access to chemical data, Nucleic Acids Res. 47 (2019) D1102–D1109, https://doi.org/10.1093/NAR/GKY1033.
[30] J.C. Shelley, A. Cholleti, L.L. Frye, J.R. Greenwood, M.R. Timlin, M. Uchimaya, Epik, A software program for pKa prediction and protonation state generation for drug-like molecules, J. Comput. Aided Mol. Des. 21 (2007) 681–691, https://doi.org/10.1007/S10822-007-9133-Z/TABLES/5.
[31] E. Wang, H. Sun, J. Wang, Z. Wang, H. Liu, J.Z.H. Zhang, T. Hou, End-point binding free energy calculation with MM/PBSA and MM/GBSA: strategies and applications in drug design, Chem. Rev. 119 (2019) 9478–9508, https://doi.org/10.1021/ACS.CHEMREV.9B00055.
[32] T.A. Halgren, R.B. Murphy, R.A. Friesner, H.S. Beard, L.L. Frye, W.T. Pollard, J. L. Banks, Glide: a new approach for rapid, accurate docking and scoring. 2. Enrichment factors in database screening, J. Med. Chem. 47 (2004) 1750–1759, https://doi.org/10.1021/JM030644S/SUPPL_FILE/JM030644S_S.PDF.
[33] R.A. Friesner, J.L. Banks, R.B. Murphy, T.A. Halgren, J.J. Klicic, D.T. Mainz, M. P. Repasky, E.H. Knoll, M. Shelley, J.K. Perry, D.E. Shaw, P. Francis, P.S. Shenkin, Glide: a new approach for rapid, accurate docking and scoring. 1. Method and assessment of docking accuracy, J. Med. Chem. 47 (2004) 1739–1749, https://doi.org/10.1021/JM0306430/SUPPL_FILE/JM0306430_S.PDF.
[34] S.S. Kesharwani, P.P. Nandekar, P. Pragyan, V. Rathod, A.T. Sangamwar, Characterization of differences in substrate specificity among CYP1A1, CYP1A2 and CYP1B1: an integrated approach employing molecular docking and molecular dynamics simulations, J. Mol. Recogn. 29 (2016) 370–390, https://doi.org/10.1002/JMR.2537.
[35] H. Yang, C. Lou, L. Sun, J. Li, Y. Cai, Z. Wang, W. Li, G. Liu, Y. Tang, admetSAR 2.0: web-service for prediction and optimization of chemical ADMET properties, Bioinformatics 35 (2019) 1067–1069, https://doi.org/10.1093/BIOINFORMATICS/BTY707.
[36] E. Krieger, R.L. Dunbrack, R.W.W. Hooft, B. Krieger, Assignment of protonation states in proteins and ligands: combining pK<Subscript>a</subscript> prediction with hydrogen bonding network optimization, Methods Mol. Biol. 819 (2012) 405–421, https://doi.org/10.1007/978-1-61779-465-0_25.
[37] C.J. Dickson, B.D. Madej, Å.A. Skjevik, R.M. Betz, K. Teigen, I.R. Gould, R. C. Walker, Lipid14: the amber lipid force field, J. Chem. Theor. Comput. 10 (2014) 865–879, https://doi.org/10.1021/CT4010307/SUPPL_FILE/CT4010307_SI_001.PDF.
[38] E. Krieger, J.E. Nielsen, C.A.E.M. Spronk, G. Vriend, Fast empirical pKa prediction by Ewald summation, J. Mol. Graph. Model. 25 (2006) 481–486, https://doi.org/10.1016/J.JMGM.2006.02.009.
[39] T. Darden, L. Perera, L. Li, L. Pedersen, New tricks for modelers from the crystallography toolkit: the particle mesh Ewald algorithm and its use in nucleic acid simulations, Structure 7 (1999) 55–60. http://biomednet.com/elecref/0969212600 7R0055. (Accessed 5 February 2022).
[40] Computer Simulation in Materials Science, 1991, https://doi.org/10.1007/978-94-011-3546-7. Computer Simulation in Materials Science.
[41] E. Krieger, G. Vriend, New ways to boost molecular dynamics simulations, J. Comput. Chem. 36 (2015) 996–1007, https://doi.org/10.1002/JCC.23899.
[42] Multivariate Calibration - Harald Martens, Tormod Næs - Google Books, n.d, https://books.google.co.in/books?hl=en&lr=&id=6lVcUeVDg9IC&oi=fnd&pg=PR13&dq=37.%09Martens,+H.%3B+N%C3%AF,+T.+Multivariate+Calibration%3B+John+Wiley+%26+Sons,+1992.&ots=ws79etXxIp&sig=vsTt93ZGmVLuoLfKBFEgVYSpfUg&redir_esc=y#v=onepage&q&f=false. (Accessed 5 February 2022).
[43] R.C. Team, R. Dc, A Language and Environment for... - Google Scholar (n.d.), https://scholar.google.com/scholar?hl=en&as_sdt=0%2C5&q=Team%2C+R.+C.%3B+DC%2C+R.+A+Language+and+Environment+for+Statistical+Computing.+Vienna%2C+Austria%3A+R+Foundation+for+Statistical+Computing%3B+2012.+URL+https%2F%2Fwww.+R-project.+org+2019.&btnG=. (Accessed 5 February 2022).
[44] Applied Spatial Data Analysis with R, Applied Spatial Data Analysis with R, 2008, https://doi.org/10.1007/978-0-387-78171-6.
[45] N. Plattner, S. Doerr, G. de Fabritiis, F. Noé, Complete protein–protein association kinetics in atomic detail revealed by molecular dynamics simulations and Markov modelling, Nat. Chem. 9 (10) (2017) 1005–1011, https://doi.org/10.1038/nchem.2785, 9 (2017).
[46] S.T. Ngo, H.M. Hung, M.T. Nguyen, Fast and accurate determination of the relative binding affinities of small compounds to HIV-1 protease using non-equilibrium work, J. Comput. Chem. 37 (2016) 2734–2742, https://doi.org/10.1002/JCC.24502.
[47] J.K.R. da Silva, P.L.B. Figueiredo, K.G. Byler, W.N. Setzer, Essential oils as antiviral agents, potential of essential oils to treat SARS-CoV-2 infection: an in-silico investigation, Int. J. Mol. Sci. 21 (2020) 3426, https://doi.org/10.3390/IJMS21103426, 21 (2020) 3426.
[48] H. Puttaswamy, H.G. Gowtham, M.D. Ojha, A. Yadav, G. Choudhir, V. Raguraman, B. Kongkham, K. Selvaraju, S. Shareef, P. Gehlot, F. Ahamed, L. Chauhan, In silico studies evidenced the role of structurally diverse plant secondary metabolites in reducing SARS-CoV-2 pathogenesis, Sci. Rep. 10 (1) (2020) 1–24, https://doi.org/10.1038/s41598-020-77602-0, 10 (2020).
[49] S. Yalçın, S. Yalçınkaya, F. Ercan, In silico detection of inhibitor potential of Passiflora compounds against SARS-Cov-2(Covid-19) main protease by using molecular docking and dynamic analyses, J. Mol. Struct. 1240 (2021), https://doi.org/10.1016/J.MOLSTRUC.2021.130556.
[50] O. Abian, D. Ortega-Alarcon, A. Jimenez-Alesanco, L. Ceballos-Laita, S. Vega, H. T. Reyburn, B. Rizzuti, A. Velazquez-Campoy, Structural stability of SARS-CoV-2 3CLpro and identification of quercetin as an inhibitor by experimental screening, Int. J. Biol. Macromol. 164 (2020) 1693–1703, https://doi.org/10.1016/J.IJBIOMAC.2020.07.235.
[51] R.M.L. Colunga Biancatelli, M. Berrill, J.D. Catravas, P.E. Marik, Quercetin and vitamin C: an experimental, synergistic therapy for the prevention and treatment of SARS-CoV-2 related disease (COVID-19), Front. Immunol. 11 (2020) 1451, https://doi.org/10.3389/FIMMU.2020.01451/BIBTEX.
[52] G.v. Glinsky, Tripartite combination of candidate pandemic mitigation agents: vitamin D, quercetin, and estradiol manifest properties of medicinal agents for targeted mitigation of the COVID-19 pandemic defined by genomics-guided tracing of SARS-CoV-2 targets in human cells, Biomedicines 8 (2020), https://doi.org/10.3390/BIOMEDICINES8050129. Page 129. 8 (2020) 129.
[53] D.W. Kneller, G. Phillips, H.M. O'Neill, R. Jedrzejczak, L. Stols, P. Langan, A. Joachimiak, L. Coates, A. Kovalevsky, Structural plasticity of SARS-CoV-2 3CL Mpro active site cavity revealed by room temperature X-ray crystallography, Nat. Commun. 11 (1) (2020) 1–6, https://doi.org/10.1038/s41467-020-16954-7, 11 (2020).
[54] D.W. Kneller, G. Phillips, K.L. Weiss, S. Pant, Q. Zhang, H.M. O'Neill, L. Coates, A. Kovalevsky, Unusual zwitterionic catalytic site of SARS-CoV-2 main protease revealed by neutron crystallography, J. Biol. Chem. 295 (2020) 17365–17373, https://doi.org/10.1074/JBC.AC120.016154/ATTACHMENT/2B66B26B-5431-4CE0-9E74-67356638A732/MMC1.DOCX.
[55] J.C. Ferreira, S. Fadl, A.J. Villanueva, W.M. Rabeh, Catalytic dyad residues His41 and Cys145 impact the catalytic activity and overall conformational fold of the main SARS-CoV-2 protease 3-chymotrypsin-like protease, Front. Chem. 9 (2021) 491, https://doi.org/10.3389/FCHEM.2021.692168/BIBTEX.
[56] S.O. Aftab, M.Z. Ghouri, M.U. Masood, Z. Haider, Z. Khan, A. Ahmad, N. Munawar, Analysis of SARS-CoV-2 RNA-dependent RNA polymerase as a potential therapeutic drug target using a computational approach, J. Transl. Med. 18 (2020) 1–15, https://doi.org/10.1186/S12967-020-02439-0/FIGURES/9.
[57] K. Naydenova, K.W. Muir, L.F. Wu, Z. Zhang, F. Coscia, M.J. Peet, P. Castro-Hartmann, P. Qian, K. Sader, K. Dent, D. Kimanius, J.D. Sutherland, J. Löwe, D. Barford, C.J. Russo, Structure of the SARS-CoV-2 RNA-dependent RNA polymerase in the presence of favipiravir-RTP, in: Proceedings of the National Academy of Sciences of the United States of America, 2021, p. 118, https://doi.org/10.1073/PNAS.2021946118/-/DCSUPPLEMENTAL.